Computed Phase Equilibria for Burnable Neutron Absorbing Materials for the Advanced CANDU Reactor Design

E. C. Corcoran, B. J. Lewis and W. T. Thompson
Department of Chemistry and Chemical Engineering, Royal Military College of Canada,
P. O. Box 17000, St. Forces, Kingston, Ont., Canada K7K 7B4
Phone: 613-541-6000 ext. 6081, Fax: 613-545-8341, email: Thompson-w@rmc.ca

Abstract

Burnable neutron absorbing materials are expected to be an integral part of the new fuel design for the Advanced CANDU Reactor. The neutron absorbing material is composed of gadolinia, dysprosia and yttria dissolved in an inert zirconia matrix. A thermodynamic model based on Gibbs energy minimization has been created to determine phase equilibria as a function of composition and temperature. The aqueous solubility and consequent potential release of neutron absorbing elements into the reactor coolant is calculated to be low in the case of a cladding breach. The calculations are consistent with a limited number of ambient solubility product measurements.

1 Introduction

Fundamental thermodynamics can be applied to determine the most stable phases at specific conditions of composition and temperature [1]. This approach is especially useful at high temperature where experimental work is difficult to conduct, or with multi-component systems such as the Burnable Neutron Absorber (BNA) material used in the design of the central element of the Advanced CANDU Reactor (ACR) fuel bundle [2]. As the specific material composition does not have a broad experience base, a thermodynamic model is of use to streamline composition selection, determine phase stability at reactor operation conditions, and determine solubility of the BNA in the Primary Heat Transport System (PHTS) in the case of a cladding breach (although the probability of cladding failure in CANDU reactors is very low).

This paper discusses the methodology of Gibbs energy minimization, outlines the thermodynamic data used to compute the phase model, and discusses aqueous experimentation to determine solubility products of $Gd(OH)_3$ and $Dy(OH)_3$.

2 Rare Earth Oxides (REO)

The BNA material is composed of the burnable neutron absorbing materials gadolinia (Gd_2O_3), dysprosia (Dy_2O_3), suspended in an inert zirconia (ZrO_2) and yttria (Y_2O_3) matrix. Dysprosium and gadolinium are members of the rare earth or lanthanide series of elements ($57 \leq Z \leq 71$) which is characterized by very stable 3^+ oxidation state and associated ions of similar ionic radius. Yttrium (Z=39) is sometimes included as a member of the lanthanide series of elements as well, since, although it has no "f" electrons, it does have a similar ionic radius and charge [3]. For generality, Ln will be used to represent Y, Gd and Dy).

The 3^+ oxidation state leads to the formation of the sesquioxide (Ln_2O_3). Sesquioxides generally crystallize into three structures: hexagonal, monoclinic, and cubic [3]. The cubic structure bears many similarities to cubic zirconia (cF12 or Fm-3m) which is isomorphous with the mineral CaF_2 (fluorite) [4,5] as shown in Figure 1a.

Cubic Ln_2O_3 (cF80 or Ia-3) has a similar structure to cubic zirconia (when $1/8^{th}$ of the structure is compared). The Ln^{3+} ions have radii similar to Zr^{4+} ions and therefore may occupy the same position. To maintain charge neutrality, one quarter of the oxide ion sites are vacant in pure cubic Ln_2O_3. These vacancies appear in a three-dimensional periodic pattern which distorts the placement of oxide ions (that would otherwise be a fluorite pattern) [3]. To capture the periodic pattern in pure cubic Ln_2O_3, the unit cell must be extended to 80 atoms accounting for the large difference in the atoms per unit cell (evident by the Pearson symbol).

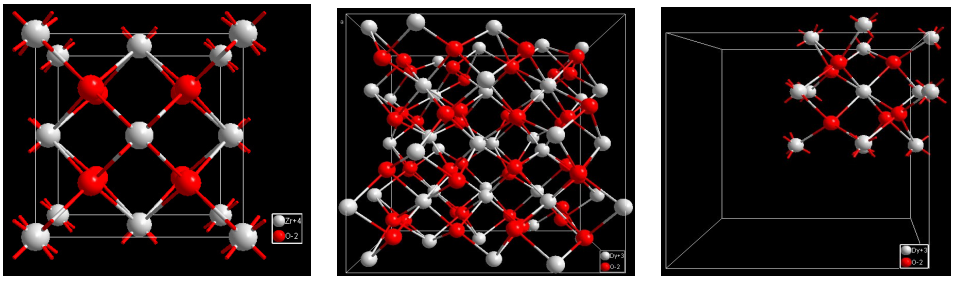

(a) **(b)** **(c)**

Figure 1. (a) Fluorite structure of ZrO_2 (Pearson symbol cF12), (b) Bixbyite structure of gadolinium oxide (Pearson symbol cF80), (c) $1/8^{th}$ Bixbyite unit cell. Lighter atoms represent Zr^{4+} or Ln^{3+} ions respectively; darker atoms represent O^{2-} ions. Note that the distortion of the oxide plane in (c) compared to (a) is caused by the periodic absence of O^{2-} ions to accommodate change neutrality [6].

3 Multi-Component Oxide Systems

In cubic solid oxide solutions of ZrO_2 and Ln_2O_3, Zr^{4+} and Ln^{3+} ions interchange on cation lattice sites. The difference in charge affects the number and placement of vacancies throughout the crystal structure. This has a direct (although small) effect on the Gibbs energy of the system, which affects the thermodynamic stabilities of the cubic solid solution relative to other potential phases at comparable conditions of temperature and pressure.

It is convenient to select the formula mass of the lanthanide sesquioxide as $LnO_{1.5}$ instead of Ln_2O_3. The mole fraction of $LnO_{1.5}$ and Ln_2O_3 is related by

$$X_{LnO_{1.5}} = \frac{2X_{Ln_2O_3}}{(1+X_{Ln_2O_3})} \quad (1)$$

Because of the potential confusion in representing composition, the computed binary phase diagrams shown subsequently include three scales: mole fraction (X) of $LnO_{1.5}$, mole fraction (X) of Ln_2O_3, and weight percent ($wt\%$).

4 Binary Systems

Phase diagrams are stability maps defining the domains of each phase, using in this case composition and temperature co-ordinates. The topology of these diagrams requires that single-phase domains be separated by two-phase regions. Only at critical temperatures may these phases co-exist. The hydrostatic pressure is set at 1 atm although this variable is of little consequence unless the pressure variation is extreme (several kbars). To illustrate the thermodynamic fundamentals [7], ZrO_2-$GdO_{1.5}$ will be considered at 2500°C where only cubic and liquid phases may exist.

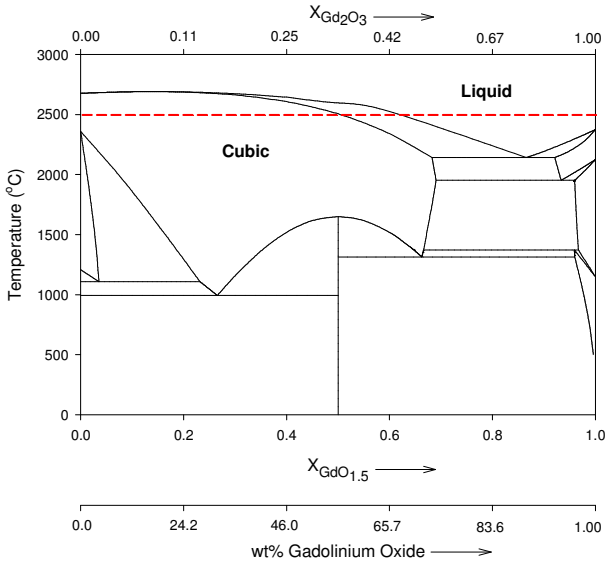

Figure 2. Binary phase diagram for ZrO_2 and $GdO_{1.5}$. Dashed line highlights the isotherm at 2500°C.

The most stable phase(s) may be determined by the process of Gibbs energy minimization. The phase(s) present at a given temperature and overall composition must provide the lowest Gibbs energy (G) for the system as a whole. For a binary system, the change in the Gibbs energy resultant from mixing (dissolution) may be viewed as the

summation of an ideal mixing term (ΔG_{ideal}) and an excess Gibbs energy term (G^E) [1] for the solution formation process from the oxide components:

$$X_{ZrO_2} ZrO_2 + X_{GdO_{1.5}} GdO_{1.5} = (ZrO_2 - GdO_{1.5})_{Solution} \quad (2)$$

The ideal mixing term assumes cations [Zr^{4+}, Gd^{3+}] in the binary system randomly interchange on similar lattice sites. For one mole of solution, the ideal mixing may be represented by [1]:

$$\Delta G_{ideal} = X_{ZrO_2} RT \ln X_{ZrO_2} + X_{GdO_{1.5}} RT \ln X_{GdO_{1.5}} \quad (3)$$

where X_{ZrO_2} and $X_{GdO_{1.5}}$ are the mole fractions of ZrO_2 and $GdO_{1.5}$, respectively, R is the ideal gas constant, and T is the absolute temperature (K). The ideal mixing term for the distribution of O^{2-} ions and vacancies has been neglected since the distribution of oxide vacancies is in a large measure related to the placement of Ln^{3+}. The ideal mixing term overlooks the thermal effects associated with mixing. To adjust the Gibbs energy for any departure from the ideal term, an excess (G^E) term is added. The excess Gibbs energy may be represented as an empirical series [1]:

$$G^E = X_{ZrO_2} X_{GdO_{1.5}} (p_o + p_1 X_{GdO_{1.5}} + p_2 X_{GdO_{1.5}}^2 + \ldots) \quad (4)$$

where the coefficients p_n (n=0,1,2…) may be functions of temperature (often linear). For simplification, the empirical series in Equation 4 can be truncated to:

$$G^E = p_o X_{ZrO_2} X_{GdO_{1.5}} \quad (5)$$

where p_o is a constant. These are sometimes called “regular” solutions [1]. The Gibbs energy curves can be constructed for the cubic and liquid phases at 2500°C and 1 atm as functions of $X_{GdO_{1.5}}$ with an appropriate value of p_o for each phase. Combined with a knowledge of the Gibbs energy difference between the cubic and liquid phases of the pure component oxides, the Gibbs energy curves for the cubic and liquid phases appear as shown in Figure 3.

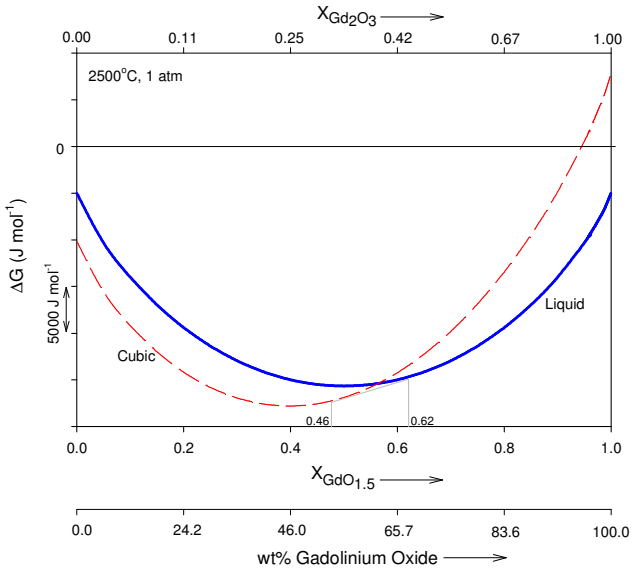

Figure 3. Gibbs energy curves for cubic and liquid phases at 2500°C and 1 atm.

The methodology of Gibbs energy minimization implies that the phase with the lower Gibbs energy at a given temperature and composition is most stable [1]. However, it is to be noted, between the line of common tangency running from 0.46 to 0.62 $X_{GdO_{1.5}}$, two phases are actually slightly more stable then either one separately. This observation is consistent with the two phase region shown in Figure 2 at 2500°C.

4.1 Binary Phase Diagrams

The thermodynamic methodology previously described can be expanded to include all of the phases present in the binary system (these include: monoclinic, hexagonal, tetragonal, bixbyite, as well as stoichometric oxide compounds). Excess mixing parameters are tuned to provide selected critical features in the latest accepted version of the phase diagram. This approach does not preclude using measurements of the Gibbs energy of mixing or related properties but sufficient information of this type with the high accuracy required is not currently available. The process applied to the modelling of the ZrO_2-$GdO_{1.5}$ binary system can also be adapted to the ZrO_2-$DyO_{1.5}$ and ZrO_2-$YO_{1.5}$ binary systems. The resultant diagrams are summarized in Figure 4.

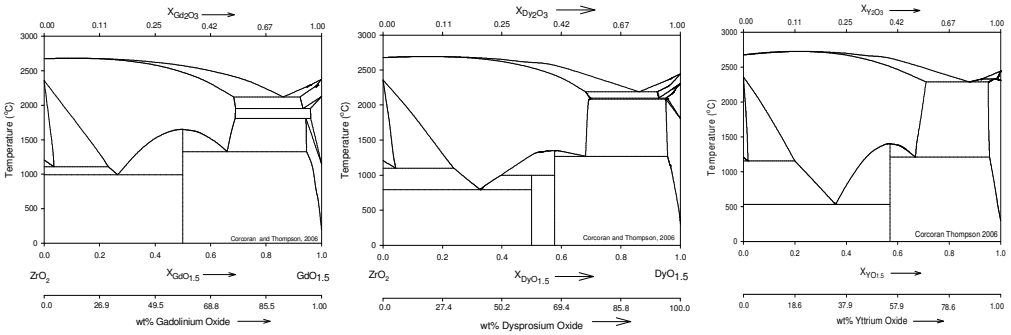

(a) **(b)** **(c)**

Figure 4. (a) ZrO_2-$GdO_{1.5}$ binary model developed to match Lakiza [8], (b) ZrO_2-$DyO_{1.5}$ binary model developed to match Yokokawa [9], (c) ZrO_2-$YO_{1.5}$ binary model developed to match Yokokawa [9].

5 Estimated Phase Equilibrium of the Quaternary System

The parameters needed to generate the three phase diagrams in Figure 4 can be incorporated into one overall treatment by the interpolation method attributed to Toop [10]. The ideal term is expanded to

$$\Delta G_{mix}^{ideal} = X_{ZrO_2} RT \ln(X_{ZrO_2}) + X_{GdO_{1.5}} RT \ln(X_{GdO_{1.5}}) + X_{DyO_{1.5}} RT \ln(X_{DyO_{1.5}}) + X_{YO_{1.5}} RT \ln(X_{YO_{1.5}}) \quad (6)$$

The Toop interpolation for the excess term is expanded for the four binary sub-systems [1]*

$$\Delta G_T^E = \left(\frac{X_{GdO_{1.5}}}{X_{GdO_{1.5}} + X_{DyO_{1.5}} + X_{YO_{1.5}}}\right) G^E_{ZrO_2-GdO_{1.5}} + \left(\frac{X_{DyO_{1.5}}}{X_{GdO_{1.5}} + X_{DyO_{1.5}} + X_{YO_{1.5}}}\right) G^E_{ZrO_2-DyO_{1.5}} + \left(\frac{X_{YO_{1.5}}}{X_{GdO_{1.5}} + X_{DyO_{1.5}} + X_{YO_{1.5}}}\right) G^E_{ZrO_2-YO_{1.5}} + (X_{GdO_{1.5}} + X_{DyO_{1.5}} + X_{YO_{1.5}})^2 G^E_{GdO_{1.5}-DyO_{1.5}-YO_{1.5}} \quad (7)$$

The phases and their proportions were computed at a particular composition over a range of temperatures and are represented on a bar graph (in which the oxides of Y, Gd, and Dy are grouped together as Ln in the resultant phases) in Figure 5. The collective treatment of Y, Gd and Dy in this way rests on the chemical similarity of these elements. The situation showing three phases over a range of temperatures at 700°C and below is a consequence of additional degrees of freedom for a system with more than two components.

* Where the $G^E_{GdO_{1.5}-DyO_{1.5}-YO_{1.5}}$ term is zero; ideal mixing is assumed for the mixing of Y^{3+}, Gd^{3+} and Dy^{3+}

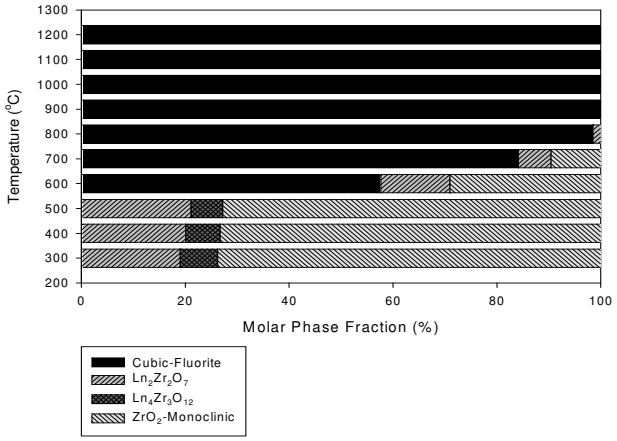

Figure 5. Phase compositional bar graph in mole percent for an 80 mol% ZrO_2, 6.67 mol% $YO_{1.5}$, 6.67 mol% $GdO_{1.5}$, and 6.67 mol% $DyO_{1.5}$.

6 Aqueous Solubility of Lanthanides

In the case of a cladding breach of the central element, ACR-BNA would be in contact with the coolant. Although it is believed that lanthanide solubility in CANDU coolant conditions (~300°C, pH~10.2, corrected to 25°C) is small, an effort has been made to create a preliminary thermodynamic model to project BNA solubility (particularly Gd^{3+} and Dy^{3+}) as a function of temperature and pH.

In principle, lanthanide oxides are soluble in acidic conditions yielding aqueous Ln^{3+} ions. In alkaline conditions, solid hydroxides $Ln(OH)_3$ suppress the solubility of Ln^{3+} ions as evident in the computed Pourbaix diagrams in Figure 6.

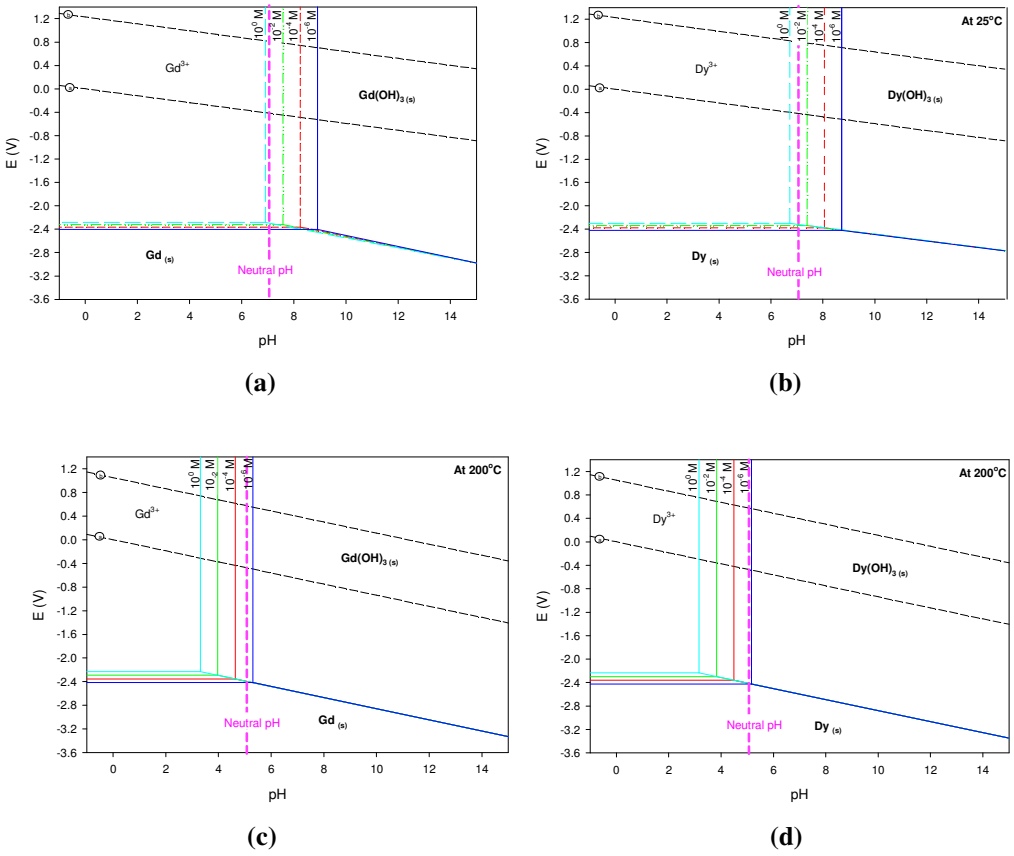

Figure 6. Calculated Pourbaix diagrams based on [11-13].
(a) and (b) are the diagrams for Gd and Dy at 25°C, respectively. (c) and (d) are the diagrams for Gd and Dy at 200°C, respectively. The condition of neutral pH is shifted to a lower value as temperature increases.

The figures show that the concentration of Ln^{3+} is only dependent on the pH of $Ln(OH)_3$ saturation solutions. Redox potentials falling between the extremes of oxygen (a) and hydrogen (b) saturations have no influence.

To confirm the low solubility at alkaline conditions implied by Figure 6, anhydrous lanthanide oxides were digested in 0.15 to 0.30 M solutions of nitric acid. A lithium hydroxide (LiOH) solution (~$2x10^{-3}$ mol mL^{-1}) was then added systematically and the pH was measured. A typical experimental result is shown in Figure 7.

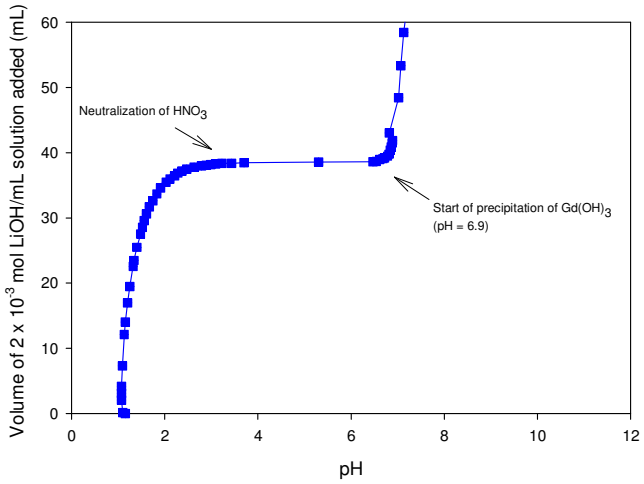

Figure 7. Titration results of an initial 8770 ppm solution of Gd^{3+}.

The solubility product, K_{sp}

$$Ln(OH)_{3(s)} \rightarrow Ln^{3+}_{(aq)} + 3(OH)^{-}_{(aq)} \tag{8}$$

was determined from the initial lanthanide ion concentration adjusted for the dilution effect of the LiOH solution addition.

$$K_{sp} = [Ln^{3+}{}_{(aq)}][OH^{-}{}_{(aq)}]^3 \tag{9}$$

where the molar OH^- concentration is related to the pH (at ambient temperature) via

$$[OH^-] = 10^{pH-14} \tag{10}$$

The results are summarized in Table 1.

Table 1. Summary of results for experimental aqueous solubility study

Lanthanide Ion ($Ln^{3+}_{(aq)}$)	Initial Ln^{3+} Concentration (ppm)	Critical pH ($Ln(OH)_3$ ppte)	K_{sp} (expressed in molar concentration)
Gd^{3+}	8770	6.9	2.4×10^{-23}
Gd^{3+}	341	7.4	3.4×10^{-23}
Gd^{3+}	341	7.3	1.7×10^{-23}
Dy^{3+}	8820	6.7	0.7×10^{-23}
Dy^{3+}	8580	6.6	0.4×10^{-23}
Dy^{3+}	3550	6.9	1.1×10^{-23}
Dy^{3+}	355	7.3	1.5×10^{-23}
Dy^{3+}	355	7.3	1.2×10^{-23}
Dy^{3+}	355	7.1	0.4×10^{-23}
Dy^{3+}	355	7.3	2.3×10^{-23}

For $Gd(OH)_3$, the average solubility product at ambient temperature was:

$$K_{sp} \approx 3.0 \times 10^{-23} \quad (11)$$

For $Dy(OH)_3$, the average solubility product at ambient temperature was:

$$K_{sp} \approx 1.0 \times 10^{-23} \quad (12)$$

The slightly greater solubility of Gd^{3+} over Dy^{3+} under comparable conditions of pH is evident in Figure 6 (a) and (b). Projections of the concentration of Gd^{3+} and Dy^{3+} at a pH of 10 with these solubility products give exceedingly low values (in the order of 10^{-6} ppm). Attempts to make a direct measurement of Ln^{3+} concentration at this pH using Neutron Activation Analysis (NAA) of solutions saturated with $Ln(OH)_3$ gave concentrations of approximately 10 and 1 ppm (for Gd^{3+} and Dy^{3+} respectively). This discrepancy could be attributed to suspended $Ln(OH)_3$ particles. It is also possible that ions of the type $Ln(OH)_x^{(3-x)+}$ may contribute to the solubility. In any event, the concentration of Ln^{3+} ions at CANDU reactor coolant conditions is expected to be very low.

Thermogravimetric Analysis (TGA) of the precipitate was performed to support the existence of $Ln(OH)_3$ precipitates in alkaline solution. For this study, samples of washed $Ln(OH)_3$ precipitates were dried at 220ºC in a controlled atmosphere of N_2 bubbled through ice water to prevent the undesired decomposition of $Ln(OH)_3$ as supported by a near constant weight after 10 hours. The samples were afterwards slowly heated to 750ºC.

The percentage mass loss for $Dy(OH)_3$ and $Gd(OH)_3$ decomposition appears in Table 2. The percentage is compared with the stoichiometric loss based on

$$2Ln(OH)_{3(s)} \rightarrow Ln_2O_{3(s)} + 3H_2O_{(g)} \quad (13)$$

Table 2. Comparison of theoretical percentage mass loss to measured results for the decomposition of lanthanide hydroxide.

Precipitate	Theoretical Mass Loss (%)	Measured Mass Loss (%)
$Dy(OH)_3$	13	14
$Gy(OH)_3$	13	14

7 Calculated Solubility of BNA Material at CANDU Reactor Operation Conditions

With some experimental corroboration of the very low solubility products for $Gd(OH)_3$ and $Dy(OH)_3$, calculations using Gibbs energy minimization methods were performed to project ionic concentrations to reactor conditions (~300°C, ~100 atm, pH ~10.2 at 25°C). The calculations are based on the belief that a thin surface layer of the BNA material will be converted to form hydroxide when contacted with water at high pressure. Furthermore, the calculations are based on extrapolated partial molar entropies and heat capacities which determine the way Gibbs energies vary with temperature. In view of the chemical similarities of Ln^{3+}, the precipitate is treated as an ideal solid solution of the type $(Y,Gd,Dy)(OH)_3$. As expected, the projected Ln^{3+} ionic concentrations are extremely low; the zirconia is more soluble as $HZrO_3^-$.

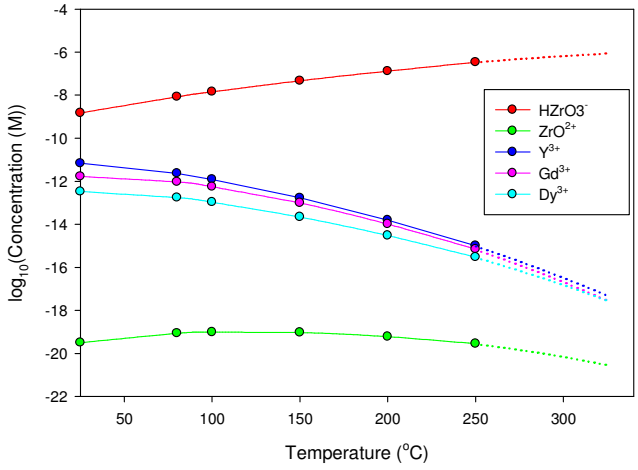

Figure 8. Calculated concentrations as a function of temperature for pH fixed at 10.2 (25°C).

8 Summary

This work describes thermodynamic treatments for the binary temperature composition phase diagrams of zirconia – gadolinia, zirconia – dysprosia, and zirconia – yttria. These phase diagrams were incorporated into a quaternary model using a Toop interpolation. The expected conditions of temperature and composition where the cubic solid solution phase is thermodynamically stable are provided. Calculations indicate that the aqueous solubility of Gd^{3+} and Dy^{3+} are very low in alkaline CANDU coolant as supported by a few measurements at ambient temperature. Phase stability and solubility are discussed in relation to reactor conditions.

9 Acknowledgements

The authors thank P. Boczar, L. Dickson, Z. He, P. Reid, R. Verrall, F. Akbari, J. Mouris, H. Hamilton, and J. Hood, all of AECL, for their continued support and encouragement. The authors acknowledge the suggestion of Prof. P. Tremaine on the possible presence of complex ions of Ln^{3+} in alkaline solutions. The authors also recognize A. Blackier and G. Bruni for their experimental assistance. The authors wish to remember especially the contributions of the late Dr. Faramarz Akbari which extended into many subject areas related to this project. He will be missed.

10 References

1. A. Pelton, and W. T. Thompson, Phase Diagrams, *Progress in Solid State Chemistry*, 10, 3, 119-155, (1975).
2. J. Hood, F. Akbari, Z. He, P. Reid, E. C. Corcoran, B. J Lewis, and W. T. Thompson, ZrO_2-Re_2O_3 Phase Stability Program in Support of ACR-1000® Fuel Design, *29th CNS Conference. Toronto, Ontario, Canada, June 1-4, (2008).*
3. G. Adachi, and Z. C. Kang, Binary Rare Earth Oxides, Kluwer Academic Publishing (2004).
4. W. B. Pearson, A Handbook of Lattice Spacings and Structures of Metals and Alloys, Pergamon, 1,(1958), 2,(1967).
5. K. Clausen, W. Hayes, J.E. MacDonald, P. Schnabel, and M.T. Hutchings, *Inorganic Crystal Structure Database, (ICSD) ICSD-77701.*
6. K. Branderburg, Diamond 3.1a Crystallographic Software. *Crystal Impact GbR. Bonn, Germany. (1997-2005).*
7. C. H. P. Lupis, Chemical Thermodynamics of Materials, North-Holland, (1983).
8. S. Lakiza, O. Fabrichnaya. C. Wang, M. Zinkevich, and F. Aldinger., Phase Diagrams of the ZrO_2-Gd_2O_3-Al_2O_3 System, *Journal of the European Ceramic Society,* 26, 233-246,(2006).
9. H. Yokokawa, N. Sakai, T. Kawada, and M. Dokiya, Phase Diagram Calculations for ZrO_2 Based Ceramics: Thermodynamic Regularities in Zirconate Formation and Solubilities of Transition Metal Oxides, *5th International Conference in Science and Technology. Melbourne, Australia, August 16-21, 59-68,(1992).*
10. G. W. Toop, Predicting Ternary Activities Using Binary Data, *Transactions of the American Institute of Mining, Metallurgical and Petroleum Engineers* 233, 5, 850-855, (1965).
11. I. Barin, O. Knacke, and O. Kubaschewski, Thermochemical Properties of Inorganic Substances, Springer-Verlag, Berlin, (1977).
12. H.E. Barner and R.V. Scheuerman, Handbook of Thermochemical Data for Compounds and Aqueous Species, Wiley-Interscience, New York, (1978).
13. M. Pourbaix, Atlas of Electrochemical Equilibria in Aqueous Solutions, Pergamon of Canada Ltd. (1966).